The evolution of whole-brain turbulent dynamics during recovery from traumatic brain injury

Noelia Martínez-Molina[1,2,3*], Anira Escrichs[1*], Yonatan Sanz-Perl[1], Aleksi J. Sihvonen[2,3,4], Teppo Särkämö[2,3], Morten L. Kringelbach[5,6,7], Gustavo Deco[1,8]

[1] Computational Neuroscience Group, Center for Brain and Cognition, Department of Information and Communication Technologies, Universitat Pompeu Fabra, Barcelona, Catalonia, Spain
[2] Cognitive Brain Research Unit, Department of Psychology and Logopedics, Faculty of Medicine, University of Helsinki, Helsinki, Finland
[3] Centre of Excellence in Music, Mind, Body and Brain, University of Helsinki, Helsinki, Finland
[4] School of Health and Rehabilitation Sciences, Queensland Aphasia Research Centre and UQ Centre for Clinical Research, The University of Queensland, Brisbane, Australia
[5] Centre for Eudaimonia and Human Flourishing, Linacre College, University of Oxford, Oxford, UK
[6] Department of Psychiatry, University of Oxford, Oxford, UK
[7] Center for Music in the Brain, Department of Clinical Medicine, Aarhus University, Aarhus, Denmark
[8] Institució Catalana de la Recerca i Estudis Avançats (ICREA), Barcelona, Catalonia, Spain

* These authors share first authorship

Corresponding author: noelia.martinez@upf.edu

Highlights

- Whole-brain turbulent dynamics capture longitudinal changes after TBI during one-year recovery period
- TBI patients show partial recovery of resting state network dynamics at large spatial scales
- Whole-brain computational modeling provides a mechanistic link between structural disconnection and recovery

Abstract

Significant advances in non-linear dynamics and computational modeling have opened up the possibility of studying how whole-brain dynamics may be impacted by brain injury. Importantly, by looking at the local level of synchronization, it is possible to obtain a comprehensive characterization of the spatiotemporal patterns affected at different spatial scales. In the current study, we applied the turbulent dynamics framework to investigate the temporal evolution in whole-brain dynamics using an open access resting state fMRI dataset from a cohort of moderate-to-severe traumatic brain injury (TBI) patients and healthy controls (HC). We first examined how several measures related to turbulent dynamics differ between HCs and TBI patients at 3-, 6- and 12-months post-injury. We found a significant reduction in these empirical measures after TBI, with the largest change at 6-months post-injury. Next, we built a Hopf whole-brain model with coupled oscillators and conducted *in silico* perturbations to investigate the mechanistic principles underlying the reduced turbulent dynamics found in the empirical data. This revealed a shift to lower coupling parameters in the TBI dataset and, critically, decreased susceptibility and information encoding capability. These findings confirm the potential of the turbulent framework to characterize whole-brain dynamics after TBI and suggest a mechanistic link between structural disconnection and impaired information processing.

Keywords— whole-brain modeling, resting state fMRI, turbulent dynamics, traumatic brain injury, *in silico* brain stimulation

1. Introduction

There has been a growing interest in the development and application of large-scale, non-linear brain modeling methods to resting state functional magnetic resonance imaging (fMRI) data (Breakspear, 2017; Cabral et al., 2014; Deco et al., 2018; Deco et al., 2019; Deco & Kringelbach, 2014; Deco et al., 2021; Deco et al., 2015; Kringelbach & Deco, 2020) as it offers whole-brain coverage and can be acquired in patient populations who are unable to perform cognitive tasks (Demertzi et al., 2015; Escrichs et al., 2022; López-González et al., 2021). Importantly, these methodological advancements have enabled reconceptualizing existing measures of non-linear dynamics in order to explain the complex dynamics of human brain activity. One prominent example is turbulence, which has been recently demonstrated in the healthy brain (Cruzat et al., 2022; De Filippi et al., 2021; Deco & Kringelbach, 2020) and in patients with a disorder of consciousness following brain injury (Escrichs et al., 2022). In this study, we combine a turbulent dynamics framework (model-free) with a computational modeling approach (model-based) to characterize whole-brain dynamics in moderate-to-severe traumatic brain injury (TBI) patients during a one-year recovery period.

Traumatic brain injury is associated with a wide range of cognitive deficits, such as attentional or memory impairments or executive dysfunction, that are often persistent, contribute to poor functional outcomes and have a profound impact on the quality of life of the patients (McAllister et al., 2004; Ponsford et al., 2014). The emergence of cognitive function in the brain is contingent on the integrity of the structural connectome, especially long-range white matter connections that contribute to the small-world topology underlying the spatiotemporal dynamical patterns observed in a healthy regime (Bassett & Bullmore, 2006). Diffuse axonal injury (DAI) has been considered one of the main mechanisms of TBI (Jolly et al., 2021), leading to disturbances in long-range connections and ultimately disrupting the spatiotemporal properties of functional brain networks (Caeyenberghs et al., 2014; Hellyer et al., 2013; Jilka et al., 2014; Kinnunen et al., 2011). Such structural and functional disruption results in long-term cognitive impairment (Bonnelle et al., 2011; Jilka et al., 2014; Kinnunen et al., 2011) and may play a role in the progressive neurodegeneration associated with TBI (Sharp et al., 2014). Nevertheless, reliable biomarkers accurately predicting cognitive outcomes after TBI have not been recognized (National Academies of Sciences et al., 2022). Here, resting state fMRI-based measures like turbulence could be clinically relevant as they can be assessed repeatedly without a specific cognitive task (De Filippi et al., 2021; Deco & Kringelbach, 2020; Escrichs et al., 2022). Despite its clinical relevance, a better understanding of how TBI affects whole-brain dynamics longitudinally is still needed.

The shift towards describing the impact of brain injury in terms of changes in whole-brain dynamics holds great promise to bestow a common framework not only to characterize cognitive deficits after TBI but, more generally, to provide insights into the mechanistic principles that support brain function. One widely used approach to studying whole-brain dynamics is based on metastability, a dynamical regime where brain regions engage and disengage flexibly over time showing transient dynamical patterns (Friston, 1997; Shanahan, 2010; Tognoli & Kelso, 2014). In the context of TBI, recent evidence has shown that patients had reduced global and network-level metastability compared to controls (Hellyer et al., 2015). Critically, this reduction was associated with cognitive impairment and damage to structural connectivity suggesting that metastability may act as a conceptual bridge between brain structure and behavior (Tognoli & Kelso, 2014). However, the concept of metastability measured as the variability over time of the global level of synchronization of the brain, commonly known as the global Kuramoto order parameter of a dynamical system, is limited as it cannot dissociate the dynamical patterns occurring at local spatial scales.

Recently, we have proposed an extension of metastability to account for such limitation based on turbulence theory developed first for fluid dynamics and since extended to other domains. As shown by Kuramoto (Kuramoto, 1984), coupled oscillators can be used to describe synchronization globally through metastability (Cabral et al., 2014; Deco, Kringelbach, et al., 2017) and to capture turbulence using a measure of local metastability (Kawamura et al., 2007). By combining Kuramoto's framework with Kolmogorov's concept of structure functions, turbulence can be calculated locally at different spatial scales in an analogy to the rotational vortices found in fluid dynamics. By taking this approach, we have found long-range correlations in higher-order task-specific regions that could be controlling a functional resting state core involving primary sensory regions (Deco & Kringelbach, 2020). Further, the results from the whole-brain computational model indicated that turbulence is a good index of the information processing capability of the brain as both reached the maximum level at the optimal fitting of the model. When applied to a population of patients with disorders of consciousness —which is often altered in severe cases of TBI— turbulence was significantly reduced at large and intermediate distances, as was the sensitivity of the brain to respond to external perturbations (Escrichs et al., 2022). Therefore, the question arises as to whether similar alterations in whole-brain dynamics could be found after TBI, across different stages of recovery.

Here, by combining empirical and computational approaches, we investigated how whole-brain dynamics are affected by TBI measured at three time points (3-, 6- and 12-months post-injury) across one year. To do so, we used a publicly available resting state fMRI dataset of patients with

moderate-to-severe TBI (N=14) and age-matched healthy individuals (N=12) and extracted the time series from each of the 1,000 parcels in the fine-grained Schaefer parcellation (Schaefer et al., 2018). We tested the hypotheses that whole-brain amplitude turbulence would (i) accurately differentiate patients with TBI from healthy controls (HC) and (ii) progressively approach the values of HCs across the one-year recovery trajectory. Furthermore, we expected to see other measures derived from the turbulent dynamics framework to discriminate between TBI patients and HCs. Finally, we anticipated that the whole-brain computational model would demonstrate that the brain's capability to respond to external *in silico* perturbations is compromised after TBI.

2. Methods

2.1. Model-free approach

2.1.1. Participants

The source of data for this study (Fig.1a) was obtained from the open access repository OpenNeuro (accession number ds000220). Please refer to the original publication (Roy et al., 2017) for a full description of the participants included. Briefly, 14 patients with moderate-to-severe TBI between the ages of 18 and 36 with education ranging from 12 to 18 years, and 12 healthy controls (HC) of comparable age and education were included. A Glasgow Coma Scale (GCS) at time of injury was indicative of severe (3-8) and moderate (9-12) injury. The NIfTI images from 2 TBI patients were discarded due to incorrect labels (superior-inferior swap) as shown in FSLeyes. All subjects with TBI completed three separate sessions (3-, 6-, and 12-months following injury). Resting state fMRI (rs-fMRI) data from HCs at baseline was also included for group comparisons.

2.1.2. Resting state fMRI acquisition

Five-minute rs-fMRI data were acquired using either a Philips Achieva 3T scanner in the Department of Radiology at Hershey Medical Center, Hershey, PA (TBI n = 1; HC n = 6) or one of two identical Siemens Magnetom Trio 3T scanners [one at the Social, Life, and Engineering Sciences Imaging Center at the Pennsylvania State University in University Park, PA (TBI n = 1, HC =4); the other at the Department of Radiology at Hershey Medical Center in Hershey, PA (TBI n = 12; HC n = 2)]. TBI and HC participants were divided between the scanners and, for repeated scanning, all subjects were scanned on the same machine across time points. As reported in the original publication, analysis of voxelwise temporal SNR indicated no influence of time on MRI signal. A whole-brain EPI sequence was used (150 volumes, TR=2000 ms, TE=30 ms, flip angle=90º, 240 × 240 mm field of view, 80 × 80 acquisition matrix, voxel size 1.9 x 1.9 x 4 mm). In addition, a high-resolution whole-brain T1-weighted image was acquired (voxel size 1mm^3).

2.1.3. Resting state fMRI preprocessing

Preprocessing was conducted using Statistical Parametric Mapping software (SPM12, Wellcome Department of Cognitive Neurology, University College London) running under Matlab Release 2021a (The MathWorks, Inc., Natick, MA). The first 5 volumes were removed to control for signal instability. Preprocessing steps included slice timing correction, realignment, segmentation, functional to structural coregistration, spatial normalization (voxel size $2mm^3$), and smoothing (8mm Gaussian kernel).

We then applied a denoising pipeline in order to minimize the variability due to physiological, outlier, and residual subject-motion effects (Nieto-Castanon, 2020). The preprocessed output files from SPM were imported into the CONN toolbox version 20.b (https://www.nitrc.org/projects/conn), including the following subject- and session-specific files: T1 and rs-fMRI scans; segmented grey matter (GM), white matter (WM), and cerebrospinal fluid (CSF) images; and 6 realignment parameters after rigid body motion correction. We applied the same pipeline as in our previous publication with TBI patients (Martínez-Molina et al., 2022). In essence, outlier scans were identified in the CONN toolbox as those that exceeded 3 standard deviations in z-scores from the global BOLD signal or with linear subject motion that exceeded 2mm. Next, we used the default denoising pipeline in the CONN toolbox with linear regression of potential confounding effects in the BOLD signal by implementing an anatomical component-based noise correction procedure (aCompCor), including the following: noise components from cerebral WM and CSF areas; estimated subject-motion parameters plus their first-order derivatives; identified outlier scans; and constant and first-order linear session effects. After evaluation of the denoised outputs (residual BOLD time series), the number of noise components extracted from the WM was increased to 10. The 1,000 nodes Schaefer parcellation in MNI152 volumetric space (Fig.1b) was added as an atlas in the CONN toolbox to extract the timeseries from each node (Schaefer et al., 2018). The Euclidean distance between parcels' centroids from the Schaefer parcellation was also calculated as in our previous publications (Deco & Kringelbach, 2020; Escrichs et al., 2022).

2.1.4. Probabilistic tractography analysis

We used the diffusion-weighted and T2-weighted neuroimaging data from 32 participants of the HCP database, as previously reported (Deco & Kringelbach, 2020). In the HCP website, a description of the acquisition parameters is detailed (Setsompop et al., 2013). We used the Lead-DBS software package (https://www.lead-dbs.org/) for the preprocessing of tractography data (Horn et al., 2017) which, briefly, were processed by using a q-sampling imaging algorithm implemented in DSI studio (http://dsi-studio.labsolver.org). Segmentation of the T2-weighted

anatomical images and co-registering the images to the b0 image of the diffusion data using SPM12 produced a WM mask. For each individual, 200,000 fibers were sampled within the WM mask. Fibers were transformed into MNI space using the Lead-DBS software (Horn & Blankenburg, 2016). Finally, the structural connectome from the Schaefer 1,000 parcellation (Schaefer et al., 2018) were extracted using the standardized methods in the Lead-DBS.

2.1.5. Amplitude turbulence

We investigated the turbulent brain dynamics (Fig.1c) by measuring the information processing across spacetime scales with the Kuramoto local order parameter (Deco & Kringelbach, 2020; Escrichs et al., 2022). The degree of synchronization of a particular brain region (n) is characterized as a function of space ($\overline{x}$) and time (t) at a given scale (λ). The parameter λ defines the extent of the spatial distances (i.e., λ scales) where the local synchronization is assessed. High λ values represent short distances in the brain, while small λ values represent long distances in the brain [e.g. λ=0.01 (approximately 100 mm) and λ=0.3 (approximately 3 mm)].

We measured amplitude turbulence by first defining the Kuramoto local order parameter and then taking the standard deviation of the modulus across time and space. First, we define the amplitude turbulence, $R_\lambda(\overline{x},t)$, as the modulus of the Kuramoto local order parameter for a given brain region as a function of the time at each spatial scale λ:

$$R_\lambda(\overline{x},t)e^{i\vartheta_\lambda(\overline{x},t)} = k\int_{-\infty}^{\infty} d\overline{x}' G_\lambda(\overline{x}-\overline{x}')e^{i\varphi(\overline{x}',t)} \quad (1)$$

where $\varphi(\overline{x},t)$ denotes the phases of the BOLD signal data, G_λ refers to the local weighting kernel $G_\lambda(\overline{x}) = e^{-\lambda|\overline{x}|}$ and k denotes the normalization factor $[\int_{-\infty}^{\infty} d\overline{x}' G_\lambda(\overline{x}-\overline{x}')]^{-1}$. The BOLD time series were filtered with a second-order butterworth filter in the range between 0.008-0.08 Hz, where we chose the typical high pass cutoff to filter low-frequency signal drifts (Fox et al., 2005; Glerean et al., 2012) and the low pass cutoff to filter the physiological noise, which tends to dominate the higher frequencies (Fox et al., 2005; Glerean et al., 2012). We then applied the Hilbert transform in order to obtain the complex phase of the BOLD signal for each brain node as a function of time.

Local levels of synchronization at a certain λ, as a function of space ($\overline{x}$) and time (t) are defined by R_λ. We then measure the amplitude turbulence, D, as the standard deviation across nodes and time of the modulus of the Kuramoto local order parameter (R_λ):

$$D = \sqrt{\langle {R_\lambda}^2\rangle_{x,t} - \langle R_\lambda\rangle_{x,t}^2} \quad (2)$$

where the brackets $\langle\rangle_{x,t}$ denote averages across space and time.

This measure captures the brain vortex space over time, motivated from fluid dynamics and the rotational vortices (Deco & Kringelbach, 2020).

2.1.6. Information cascade flow

The information cascade flow indicates how the information travels from one scale (λ) to a lower scale (λ − Δλ, where Δλ corresponds to a scale step) in successive time steps (t and t + Δt).

In this regard, the information cascade flow captures the information transfer across scales, and is calculated as the temporal correlation between the Kuramoto local order parameter in two successive scales and times as:

$$\mathrm{F}(\lambda) = \langle \mathrm{corr_t}(\mathrm{R}_\lambda(\overline{x}, \mathrm{t} + \Delta\mathrm{t}), \mathrm{R}_{\lambda-\Delta\lambda}(\overline{x}, \mathrm{t}))\rangle_{\bar{x}} \tag{3}$$

where the brackets $\langle\rangle_{\bar{x}}$ indicate averages across time and nodes. Then the information cascade is obtained by averaging the information cascade flow across scales λ, which captures the whole behavior of the information processing across scales.

2.1.7. Information transfer

The information transfer captures how information travels across space at each λ scale. It is calculated as the slope of a linear fitting, in the log-log scale, of the temporal correlation between the Kuramoto local order parameter of two nodes at each scale as a function of its Euclidean distance (r) in the inertial subrange.

$$\log\left(\mathrm{corr_t}\left(\mathrm{R}_\mathrm{n}^\lambda, \mathrm{R}_\mathrm{p}^\lambda\right)(\mathrm{r})\right) = A^\lambda * \log(\mathrm{r}) + B^\lambda \tag{4}$$

where A^λ and B^λ are the fitting parameters for the λ scale, and r denotes the distance in the brain. The negative slope (A^λ) represents the transfer in the spatial direction r of the information in terms of temporal correlation of the local synchronization level. Thus, when the slope is more pronounced, the information travels short distances, while a flatter slope indicates that information is transferred over long distances.

2.1.8. Local node-level metastability

The node-level metastability, NLM, defines the variability of the local synchronization of the nodes and is computed as the standard deviation across time of the Kuramoto local order parameter as follows:

$$\mathrm{NLM}(\mathrm{n}, \lambda) = \sqrt{\langle \mathrm{R}_\mathrm{n}^\lambda(\mathrm{t})^2\rangle_\mathrm{t} - \langle \mathrm{R}_\mathrm{n}^\lambda(\mathrm{t})\rangle_\mathrm{t}^2} \tag{5}$$

where brackets $\langle\rangle_t$ denote average across time.

Here, we estimated the discrete version of the node-level Kuramoto order parameter, with modulus R and phase ν, which represents a spatial average of the complex phase factor of the local oscillators weighted by the coupling as:

$$R_n^{\lambda}(t)e^{i\nu_n(t)} = \sum_p \left[\frac{C_{np}^{\lambda}}{\sum_q C_{nq}^{\lambda}}\right] e^{i\varphi_p(t)} \tag{6}$$

where $\phi_p(t)$ are the phases of the spatiotemporal data and C_{nq}^{λ} is the local weighting kernel between node n and q, and λ defines the spatial scaling:

$$C_{np} = e^{-\lambda(r(n,p))} \tag{7}$$

2.2. Model-based approach

2.2.1. Whole-brain Hopf model

We built whole-brain dynamical models with Stuart-Landau oscillators based on the normal form of a supercritical Hopf bifurcation (Deco et al., 2017a). This type of bifurcation can change the qualitative nature of the solutions from a limit cycle that yields self-sustained oscillations toward a stable fixed point in phase space. This model is characterized by model parameters that rule the global dynamical behavior. One control parameter is the multiplicative factor (G) representing the global conductivity of the fibres scaling the structural connectivity between brain areas, which is assumed to be equal across the brain (Deco et al., 2017a,b). The other relevant parameters are the local bifurcation parameter (a_n), which rules the dynamical behavior of each area between noise induced ($a < 0$), self-sustained oscillations ($a > 0$), or a critical behavior between both ($a \sim 0$) (Fig.1d). The model parameters were optimized to better fit the empirical functional connectivity as a function of the distance, r, within the inertial subrange. The models consisted of 1,000 brain regions from the resting state atlas (Schaefer et al., 2018). The underlying structural connectivity matrix C_{np} was added to link the brain structure and functional dynamics by computing the exponential distance rule (Equation 7). The local dynamics of each brain region were characterized by the normal form of a supercritical Hopf bifurcation, which emulates the dynamics for each region from noisy to oscillatory dynamics as:

$$\frac{dx_n}{dt} = a_n x_n - [x_n^2 + y_n^2]x_n - \omega_n y_n + \nu\eta_n(t) \tag{8}$$

$$\frac{dy_n}{dt} = a_n y_n - [x_n^2 + y_n^2]y_n + \omega_n x_n + \nu\eta_n(t) \tag{9}$$

where $\eta_n(t)$ is the additive Gaussian noise with standard deviation $\nu = 0.01$. This normal form has a supercritical bifurcation at $a_n = 0$, such that for $a_n > 0$, the system is in a stable limit cycle oscillation with frequency $f_n = \omega_n/2\pi$, while for $a_n < 0$ the local dynamics are in a stable point (the noisy state). The frequency ω_n of each region was obtained from the empirical functional MRI data as the power spectrum peak.

Finally, the whole-brain dynamics were determined by the set of coupled equations as follows:

$$\frac{dx_n}{dt} = a_n x_n - [x_n^2 + y_n^2]x_n - \omega_n y_n + G\sum_{p=1}^{N} C_{np}\left(x_p(t) - x_n\right) + \nu\eta_n(t) \quad (10)$$

$$\frac{dy_n}{dt} = a_n y_n - [x_n^2 + y_n^2]y_n + \omega_n x_n + G\sum_{p=1}^{N} C_{np}\left(y_p(t) - y_p\right) + \nu\eta_n(t) \quad (11)$$

where the global coupling factor G was scaled equally for each brain region representing the input received in each region n from every other region p. The output of the model is a set of complex-valued BOLD-like signals with time-varying intrinsic frequencies (ω). The real part is considered to represent BOLD signal recorded in the fMRI session whereas the imaginary part characterizes the hidden state of the oscillator unseen to the scanner.

2.2.2. Functional connectivity fitting

The functional connectivity fitting of the BOLD signal data was assessed by applying Kolmogorov's structure-function. The structure-function for a variable u characterizes the evolution of the functional connectivity (FC) as a function of the Euclidean distance between equally distant brain regions and is defined as follows:

$$S(r) = \langle (u(\overline{x} + r) - u(\overline{x}))^2 \rangle_{x,t} = 2[FC(0) - FC(r)] \quad (12)$$

where FC(r) is the spatial correlations of two points separated by a Euclidean distance r, and is given by:

$$FC(r) = \langle u(\overline{x} + r)u(\overline{x}) \rangle_{x,t} \quad (13)$$

where $\langle\rangle_{x,t}$ denotes average across the spatial x coordinates of the nodes and time. Then, we calculated the fitting as the Euclidean distance between simulated and empirical FC(r) within the inertial subrange (Deco & Kringelbach, 2020).

2.2.3. Susceptibility and Information encoding capability

We used the susceptibility and information encoding capability measures in order to study how the whole-brain model reacts to *in silico* perturbations. The susceptibility measure obtains the brain's sensitivity to react to external stimulation. The Hopf model was perturbed for each G by

randomly changing the local bifurcation parameter, a_n, in the range [-0.02: 0] and was computed by measuring the modulus of the local Kuramoto order parameter as:

$$\chi = \langle\langle\langle\widetilde{R}_{\lambda_s}(\overline{x},t)\rangle_t - \langle R_{\lambda_s}(\overline{x},t)\rangle_t)\rangle_{trials}\rangle_{\bar{x}} \quad (14)$$

where $\widetilde{R}_{\lambda_s}(\overline{x},t)$ corresponds to the perturbed case, the $R_{\lambda_s}(\overline{x},t)$ to the unperturbed case, and $\langle\rangle_t$, $\langle\rangle_{trials}$ and $\langle\rangle_{\bar{x}}$ to the average across time, trials, and space, respectively.

Similarly, the Information encoding capability (I) captures how the external stimuli are encoded in whole-brain dynamics. This measure was defined as the standard deviation across trials of the difference between the perturbed $\widetilde{R}_{\lambda_s}(\overline{x},t)$ and unperturbed $R_{\lambda s}(\overline{x},t)$ mean of the modulus of the local Kuramoto order parameter across time t, averaged across all brain regions n as follows:

$$I = \sqrt{\left\langle\langle(\langle\widetilde{R}_{\lambda_s}(\overline{x},t)\rangle_t - \langle R_{\lambda_s}(\overline{x},t)\rangle_t)^2\rangle_{trials}\right\rangle_{\bar{x}} - \left\langle\langle(\langle\widetilde{R}_{\lambda_s}(\overline{x},t)\rangle_t - \langle R_{\lambda_s}(\overline{x},t)\rangle_t)\rangle^2{}_{trials}\right\rangle_{\bar{x}}} \quad (15)$$

where the brackets $\langle\rangle_t$, $\langle\rangle_{trials}$ and $\langle\rangle_{\bar{x}}$ denote the averages defined as above.

2.3. Statistical analyses

Multiple unpaired T-tests were used for the pairwise comparisons between TBI patients and controls. To correct for multiple comparisons for all computed λ, we used false discovery rate (FDR) with the method of Benjamini and Hochberg (Benjamini and Hochberg, 1995). The longitudinal effects within the TBI group were assessed with repeated measures ANOVA and post hoc comparisons.

3. Results

Our findings are split into two different approaches: model-free and model-based. In the first approach, we computed empirical measures of whole-brain dynamics using a fine-grained parcellation with 1,000 regional phase time courses derived from resting state fMRI BOLD data in both healthy controls (N=12) and patients with TBI (N=12) at 3-, 6- and 12-months post-injury (see Fig.1 and Methods for more details). First, we assessed the amplitude turbulence across different spatial scales or λ values. This parameter determines the size of the spatial distances where the synchronization is evaluated. The amplitude turbulence is defined as the standard deviation of the Kuramoto local order parameter that describes the local level of synchronization as a function of space, x, and time, t, at a given spatial scale λ. In the supplementary material, we included four videos (Supplementary Videos 1 to 4) of the full spatiotemporal evolution of Kuramoto local order parameter across time of the full resting state of a representative participant for each condition

(healthy controls and TBI at 3-, 6- and 12-months post-injury). Second, we examined how the information is transferred across space in terms of the temporal correlation between the level of local synchronization at each scale. We also measured how the information travels across scales in consecutive time steps by defining the information cascade flow. Furthermore, to summarize the information transmission's whole behavior across scales, we defined the information cascade as the information cascade flow averaged across all λ scales.

Finally, to explore the sensitivity of patients and controls to react to external *in silico* perturbations, we built a whole-brain dynamical model for each condition. We used a model based on the normal form of a supercritical Hopf bifurcation coupled with dMRI structural connectivity and the exponential distance rule. For each whole-brain model, we applied *in silico* perturbations by changing the local bifurcation parameter and computed the susceptibility and information encoding capability measures.

3.1. Model-free measures of synchronization

3.1.1. Empirical measures of turbulence are reduced after traumatic brain injury compared to healthy controls

To examine how global information processing may be impaired due to TBI, we compared amplitude turbulence and derivative measures across the whole brain between healthy controls (HCs) and moderate-to-severe TBI patients at 3-,6- and 12-months post-injury. Global amplitude turbulence was significantly reduced in TBI patients compared to HCs across all time points but with significant differences affecting different ranges of spatial scaling. After 3-months, TBI patients showed reduced turbulence compared to HCs at intermediate and large distances ($\lambda = 0.18 - 0.06$, $p < 0.05$, Fig.2a and Table S1) whereas this pattern was reversed after 12-months, with most significant differences affecting intermediate and short distances ($\lambda = 0.27 - 0.21$ and 0.15, $p < 0.05$, Fig.2c and Table S2). In other words, TBI patients at 12-months post-injury have values of amplitude turbulence at large distances that are similar to HCs. Most strikingly, after 6-months, TBI patients showed a significant reduction in turbulence across all spatial scales except for λ=0.27 with the greatest effect size at λ=0.06 (λ=0.24, $p < 0.05$ and λ=0.21-0.01, $p < 0.01$, Cohen's $d_{(\lambda=0.06)}$ =1.53, Fig.2b and Table S3). All these comparisons survived multiple comparison correction by false discovery rate (FDR; q = 0.1).

The results from the information transfer indicated that it was significantly lower in TBI patients in all time points and spanning most spatial scales except for λ=0.01 after 12-months (Fig2.d-f, Table S4-6), which corresponds to the largest spatial scale included in the present study. We did not find significant differences between HCs and TBI patients in information cascade flow after 12-

months (Fig2.g, Table S9). However, this was significantly reduced at intermediate spatial scales after 3-months (λ=0.15-0.09, $p < 0.05$, Table S7) and in most spatial scales after 6-months (λ=0.18-0.15, $p < 0.05$ and λ=0.12-0.01, $p < 0.01$, Table S8). For information cascade flow, the largest effect size was found at λ=0.06 in the HCs vs TBI after 6-months comparison (Cohen's d=1.74, Fig2.g). As expected, the significant difference in information cascade was found in the HCs vs TBI patients after 6-months post-injury comparison (Fig2.h, Table S10).

3.1.2. Empirical measures of turbulence show the greatest reduction at the 6-month stage in the longitudinal trajectory

After the strong and widespread differences in amplitude turbulence and other derivative measures found between HCs and TBI patients after 6-months post-injury, we investigated whether this stage was also showing a clear distinction in the recovery trajectory. To do so, we performed a repeated measures ANOVA with time points as within-group factor. We found a significant group effect in global amplitude turbulence at λ=0.06 ($F_{(2,22)} = 3.804$, $p = 0.0381$, $\eta^2 = 0.2570$, Fig.3a left) and λ=0.03 (($F_{(2,22)} = 3.660$, $p = 0.0424$, $\eta^2 = 0.2497$, Fig.3a right). Post hoc comparisons revealed that global amplitude turbulence was significantly decreased after 6-months compared to 12-months post-injury. Within the TBI patient group, information cascade flow showed a significant reduction for the 6-months post-injury stage compared to 3- and 12-months at λ=0.06 ($F_{(2,22)} = 5.911$, $p = 0.0088$, $\eta^2 = 0.3495$) and λ=0.03 ($F_{(2,22)} = 5.765$, $p = 0.0097$, $\eta^2 = 0.3439$). Likewise, information cascade was significantly reduced at the 6-months post-injury stage compared to 3- and 12-months ($F_{(2,22)} = 4.747$, $p = 0.0193$, $\eta^2 = 0.3014$,Fig.3b). No significant differences were found for information transfer in the within-group analysis.

3.1.3. Reductions in RSN empirical turbulence at the 6-month stage show recovery at the 12-month stage

To reduce the number of analyses and to focus on specific hypotheses, we examined the differences in turbulence between HCs and TBI patients for the time points and spatial scales in the TBI recovery trajectory where we found significant reductions in global amplitude turbulence in the within-group analysis, i.e. 6- and 12-months post-injury at λ=0.06 and λ=0.03. For the network-level analysis, we defined the node-level metastability as the standard deviation over time of the Kuramoto local order parameter for each condition and computed the mean of all constituent nodes of each resting state network (RSN). Compared to HCs, TBI patients at 6-months post-injury had decreased amplitude turbulence in all (λ=0.03) or most (λ=0.06) RSNs. The dorsal attention-, somatomotor- and control-networks (CNT) showed the largest effect size at both λ=0.06 and 0.03 (Fig.3c-d left panel and Tables S11-12). After 12-months post-injury, however, we did not detect

significant differences in amplitude turbulence for any RSNs at the spatial scales considered (Fig.3c-d right panel).

Furthermore, we computed the Kolmogorov-Smirnov distance (KSD) to quantify the difference in the distributions of node-level metastability between HCs and TBI patients. Here larger values of KSD mean more different distributions. We found that the KSD monotonically decreases across scales in all group comparisons, whereas the value of λ increases. In other words, the KSD is maximal for lower values of λ, i.e., long distances in the brain (Fig. 4a). Crucially, the highest KSD is found between HCs and TBI patients at 6-months post-injury.

For illustrative purposes, Fig. 4b displays the absolute difference in node-level metastability between HCs and TBI patients at 3-,6- and 12-months post-injury at λ= 0.03 rendered onto the brain cortex. Additionally, we computed the number of nodes on the top 15 % quantile of the absolute difference in node-level metastability for the HCs vs TBI patients at 6-months post-injury comparison (Fig. 4c left panel). This confirmed that the nodes with the largest differences in node-level metastability were located in the dorsal attention-, somatomotor- and control-networks. Further, we identified the top 10 nodes within the top 15 % quantile for these RSNs to better characterize their anatomical distribution. In this ranking, the top 10 nodes were included in the left somatomotor- and bilateral dorsal attention-networks (Fig. 4c right panel and Table S13).

3.2. Model-based framework

Next we built a whole-brain dynamical model for each condition to examine the effect of TBI on the sensitivity to respond to *in silico* external perturbations. Secondarily, we also wanted to assess how TBI impacts the value of the global coupling parameter G. Specifically, we defined a whole-brain model of coupled oscillators (Stuart-Landau oscillators) for each time point of the TBI patients and HCs rs-fMRI data. Our model was based on the normal form of a supercritical Hopf bifurcation (Deco, Kringelbach, et al., 2017) where we coupled the empirical structural connectivity (dMRI template) and the exponential distance rule (Ercsey-Ravasz et al., 2013) to the rs-fMRI data (see Methods).

To optimize the fitting between the whole-brain model and the empirical rs-fMRI data, we varied the global coupling parameter G from 0 to 3 in steps of 0.01, and for each G value, we ran 100 simulations with the same TR (2s) and time duration (145 scans) as the empirical rs-fMRI data. For the fitting function, we used Kolmogorov's concept of structure functions of a variable u, which here denotes the spatiotemporal rs-fMRI BOLD signal. Thus, the fitting of the functional connectivity was computed as the Euclidean distance between the empirical and simulated functional connectivity (FC) as a function of distance (r) within the inertial subrange (see Methods). We then determined

the optimal working point of each model as the minimum of the fitting level. Importantly, the working point of the model for the TBI patients at all time points (3-,6- and 12-months post-injury) was lower than that for the HCs (Fig.5a).

Once we identified the working point G for each rs-fMRI dataset, we introduced external perturbations by changing the local bifurcation parameter a_n of each brain node n. For each value of G, we perturbed the whole-brain model 100 times with random parameters for the local bifurcation parameter. Our model-based measures, susceptibility and information encoding capability, allowed us to evaluate the reactivity to the external perturbations introduced (see Methods). Susceptibility was estimated by first measuring the perturbed and non-perturbed modulus of the Kuramoto local order parameter and then calculating the difference between the perturbed and non-perturbed cases averaged across time, trials, and brain nodes. As an extension of this measure, the information capability of the whole-brain model was calculated as the standard deviation across trials of the difference between the perturbed and unperturbed mean of the modulus of the local order parameter across time, averaged over all brain nodes.

Fig. 5b-c shows that both susceptibility and information encoding capability were significantly reduced in the TBI sample across all time points compared to HCs (see also Table S14). Interestingly, we found the largest effect size in the comparison of HCs with TBI patients at 6-months post-injury (information encoding capability, $t_{(198)} = 23.300$, $p < 0.0001$, Cohen's d=3.28; susceptibility, $t_{(198)} = 15.420$, $p < 0.0001$ Cohen's d=2.17). This is suggesting that, at this stage, the brain is working in a regime that is the least responsive to external perturbations.

4. Discussion

Here we investigated how TBI impacts whole-brain resting state fMRI dynamics using a turbulence-based framework (Deco & Kringelbach, 2020; Deco et al., 2021). Our findings revealed specific spatial patterns of reduction in global amplitude turbulence between HCs and TBI patients at all three time points (3-, 6- and 12-months post-injury). Further, within-group comparisons indicated that the largest reduction in turbulence levels is observed after 6-months post-injury in TBI patients. The information transfer also differed between HCs and TBI patients across all spatial scales and time points. Likewise, we found significant reductions in information cascade flow (between-group comparison only) and information cascade. When analyzing network-level turbulence between HCs and TBI patients at 6-months post-injury, most RSNs showed decreased levels of turbulence. Interestingly, we could not detect any significant difference at 12-months post-injury, indicating some degree of recovery at this stage - as already hinted by the previously reported lack of cost associated with hyperconnectivity (Roy et al., 2017). Finally, the results from

the whole-brain model indicated that susceptibility and information encoding capability are reduced after TBI, with the largest effect size again in the comparison between HCs and TBI patients at 6-months post-injury. These results provide causal links needed for a better understanding of the recovery process one year after TBI. To the best of our knowledge, this is the first study to examine the temporal evolution of turbulent dynamics during recovery from TBI.

Diffuse axonal injury (DAI) is present in most severe-to-moderate TBI patients (Jolly et al., 2021), preferentially damaging long-range connections and disrupting small-world topology and large-scale functional networks (Sharp et al., 2014). Our empirical finding of reduced turbulence at large distances after TBI at 6-months post-injury as compared to HCs suggests a potential association between the presence of long-range disconnection caused by DAI and global information processing as measured with turbulence. Given that we did not analyze the individual structural connectivity in the current dataset and that there is no report on the presence of DAI, this interpretation remains speculative. However, previous work has shown that a reduction in global metastability in TBI patients is associated with loss of white matter integrity within frontal regions (Hellyer et al., 2015), which points to an important avenue for future work investigating the relationship between turbulence and structural disconnection especially in long-range association tracts. In support of this interpretation, recent work has proven that DAI affects as much as 52% of moderate-to-severe DTI patients (Jolly et al., 2021), which is the degree of severity included in the current study (Roy et al., 2017).

In addition to reduced turbulence (Fig.2a-c), we found decreased information transfer (Fig.2d-e) across space between TBI patients and HCs across all time points and for most spatial scales, though no significant difference emerged in the within-group comparison. Information cascade flow between HCs and TBI exhibited the largest effect size after 6-months post-injury (Fig.2g). Regarding information cascade, the strongest difference was also found at 6-months post-injury both in the between- and within-group comparison (Fig.2h and Fig.3b, respectively). These results provide complementary evidence for the alteration of information transmission after TBI across space within a given scale (information transfer) and across time and spatial scales (information cascade flow and information cascade). Alongside reductions in global turbulence, these empirical results align with our previous findings using a turbulent framework in patients with disorders of consciousness, some after brain injury (Escrichs et al., 2022).

Our computational findings are consistent with our empirical results, demonstrating that TBI hinders the reactivity of the brain to external *in silico* perturbations. When fitting the Hopf model to each empirical condition, we found lower values in the optimal working point for TBI patients across time points. The optimal working point adopts its value from the global coupling parameter G, which

represents the conductivity of the fiber densities among brain regions given by the underlying structural connectivity (Escrichs et al., 2022; López-González et al., 2021). Therefore, this suggests a mechanistic link between structural disconnection after TBI and whole-brain dynamics, again in keeping with our previous study showing a shift to lower values of G in patients with disorders of consciousness (Escrichs et al., 2022). Also, in line with that study, the susceptibility and information encoding capability were significantly reduced in TBI patients across time points compared to HCs. Taken together, this suggests a mechanistic link between the structural disconnection, likely caused by DAI, and whole-brain dynamics.

Importantly, the turbulent dynamics framework adopted here lends support to the graph theory results obtained in the same dataset (Roy et al., 2017) but extends those findings by offering a dynamical approach across spatial scales and a causal perspective on the information processing deficits following TBI during one year. Previously, Roy et al. (2017) have shown that global functional hyperconnectivity, in terms of network strength, peaked at 6-months post-injury. Of note, the local analysis revealed hyperconnectivity in the left frontal DMN and temporo-parietal attentional control networks across time points but only associated with an increased cost at 6-months post-injury. Moreover, a cost-efficiency analysis showed that this elevated cost was mostly due to a higher number of medium-range connections rather than long-range connections. This fits well with our finding that turbulence is reduced at large distances at 6-months post-injury (λ= 0.06 λ=0.03) with no residual effects at those spatial scales after 12-months, when there was no cost associated with hyperconnectivity. Remarkably, we also found that the 15% quantile nodes in the HCs vs. TBI patients at 6-months were in the SM, DAT and CNT networks, in accordance with increased cost found in the temporo-parietal control network by Roy et al. (2017). Overall, our findings suggest a shift in the functional plasticity of the brain in response to TBI where the turbulent dynamics at large distances rebalances to a healthy regime during the period spanning from 6 months to 12 months post-injury.

Our empirical results are based on resting state fMRI data where we found lower turbulence in TBI patients as compared to HCs across spatial states and time points and, crucially, involving large distances at 6-months post-injury. In light of these findings, two interrelated questions arise: (i) would this reduced turbulence at rest (less variability in local synchronization) imply a longer and less reliable transition to a cognitive task and (ii) would cognitive tasks show a concomitant reduction in turbulence in higher-order brain regions? These are important considerations to bear in mind since a core symptom of TBI are deficits in executive function (EF) (Miyake et al., 2000) that respond to neurorehabilitation strategies (Martinez-Molina et al., 2021; Martinez-Molina et al., 2022; Siponkoski et al., 2021; Siponkoski et al., 2020) in association with enhanced structural

connectivity (Sihvonen et al., 2022). The tasks for evaluating EF require the rapid communication across large-scale brain networks involving sensory, motor and higher-order regions (Bonnelle et al., 2011; Erika-Florence et al., 2014; Jilka et al., 2014; Sharp et al., 2010; Spreng & Grady, 2010). This intuitive link between altered information processing and executive dysfunction after TBI has already been demonstrated for global metastability (Hellyer et al., 2015). Thus, future work should address whether similar reductions in the local level of synchronization as reflected here by turbulence amplitude are correlated with cognitive impairment and can be found in tasks commonly used to evaluate cognitive outcomes after TBI.

The results from the present study have some potential clinical implications. Amplitude turbulence and other information processing-based measures might improve clinical diagnostics in TBI as they demonstrated sensitivity to the temporal changes in whole-brain dynamics after TBI compared to HCs. Further information regarding the relationship of these measures and TBI severity is still needed. However, information processing-based measures obtained from resting state data could provide a meaningful and repeatable way to monitor the evolution of TBI, the recovery progress, and the patient's possible response to treatments as these remain prominent challenges in clinical settings to date (National Academies of Sciences et al., 2022). Our *in silico* perturbation approach with the Hopf computational model also indicated reduced coupling and reactivity to external stimulation after TBI across time points. We restricted our perturbative protocol to the introduction of random values in all nodes to modify the local bifurcation parameter of the model. That being said, it would be interesting to implement an excitatory protocol for individual nodes or a subset of relevant nodes in order to identify brain targets that can be stimulated with techniques such as transcranial magnetic stimulation (TMS) (Demirtas-Tatlidede et al., 2012). Notably, some promising results indicate that TMS and neurorehabilitation may act synergistically to improve functional outcomes after TBI (Nardone et al., 2020). Yet, we leave the implementation of such perturbative protocol for future work.

It is also worthwhile to acknowledge some limitations in the current study. Although this dataset represents a relatively homogenous sample in terms of age and time since injury, it remains of small size and a replication with a larger cohort of patients is needed to assess the generalizability of these results. In addition, the resting state sequence comprised 150 scans with a temporal resolution of 2s that were acquired over a 5-minute period. While it has been shown that functional correlation of RSNs only stabilizes after 5-min with TR=2.3s (Van Dijk et al., 2010), recent evidence indicates that metastability is less affected by temporal resolution and shows greater reliability in short-term scans (Yang et al., 2021). Regarding the presence of focal lesions, Roy et al. (2017) found a lack of correlation between lesion size and network metrics. Consequently, we assumed

this could also apply to measures of turbulent dynamics. However, we did not consider the effect of focal lesions in our analysis as the lesion maps were not accessible and our results should be interpreted with caution.

In conclusion, we have shown that whole-brain turbulent dynamics complement previous findings on the temporal evolution of functional connectivity after TBI in an open access dataset of healthy controls and patients with data collected after 3-, 6- and 12-months post-injury. Specifically, our empirical results suggest the presence of maladaptive neuroplasticity at 6-months post-injury as manifested in the reduction of global amplitude turbulence at large distances. Thus, we demonstrated that the framework of turbulent dynamics may facilitate our understanding of how the brain responds to traumatic injury. Importantly, our computational approach suggests a mechanistic link between structural disconnection caused by diffuse axonal injury and impaired information processing in patients with moderate-to-severe TBI.

CRediT author statement

Noelia Martínez-Molina: Conceptualization, Formal analysis, Visualization, Writing - original draft, Project administration. **Anira Escrichs:** Software, Formal analysis and Writing - review & editing. **Yonatan Sanz-Perl:** Software and Writing - review & editing. **Aleksi J. Sihvonen:** Writing - review & editing. **Teppo Särkämö:** Writing - review & editing. **Morten L. Kringelbach:** Methodology, Visualization, Software and Writing - review & editing. **Gustavo Deco:** Supervision, Methodology, Software and Writing - review & editing.

Funding

N.M.M. was supported by the Beatriu de Pinós programme (grant agreement no. 2019-BP-00032) from the European Union's Horizon 2020 research and innovation programme under the Marie Sklodowska-Curie agreement no. 801370. A.E. is supported by the HBP SGA3 Human Brain Project Specific Grant Agreement 3 (grant agreement no. 945539), funded by the EU H2020 FET Flagship programme. Y.S.P. is supported by European Union's Horizon 2020 research and innovation program under the Marie Sklodowska-Curie grant 896354. A.J.S. is supported by Finnish Cultural Foundation (grant 191230), Orion Research Foundation and Signe and Ane Gyllenberg Foundation. T.S. is supported by Academy of Finland (grants 338448 and 346211) and European Research Council (grant 803466). M.L.K. is supported by the Center for Music in the Brain, funded by the Danish National Research Foundation (DNRF117), and Centre for Eudaimonia and Human Flourishing at Linacre College funded by the Pettit and Carlsberg Foundations. G.D. is

supported by the Spanish national research project (ref. PID2019-105772GB-I00 MCIU AEI) funded by the Spanish Ministry of Science, Innovation and Universities (MCIU), State Research Agency (AEI).

Declaration of Competing Interest

The authors declare that they have no known competing financial interests or personal relationships that could have appeared to influence the work reported in this paper.

Code availability statement

All code written in support of this study is publicly available on
https://github.com/noechan/TBI_ON_turbu_Hopf_NC

References

Bassett, D. S., & Bullmore, E. (2006). Small-world brain networks. *Neuroscientist*, *12*(6), 512-523.

Bonnelle, V., Leech, R., Kinnunen, K. M., Ham, T. E., Beckmann, C. F., De Boissezon, X., Greenwood, R. J., & Sharp, D. J. (2011). Default mode network connectivity predicts sustained attention deficits after traumatic brain injury. *J Neurosci*, *31*(38), 13442-13451.

Breakspear, M. (2017). Dynamic models of large-scale brain activity. *Nature Neuroscience*, *20*(3), 340-352.

Cabral, J., Luckhoo, H., Woolrich, M., Joensson, M., Mohseni, H., Baker, A., Kringelbach, M. L., & Deco, G. (2014). Exploring mechanisms of spontaneous functional connectivity in MEG: how delayed network interactions lead to structured amplitude envelopes of band-pass filtered oscillations. *Neuroimage*, *90*, 423-435.

Caeyenberghs, K., Leemans, A., Leunissen, I., Gooijers, J., Michiels, K., Sunaert, S., & Swinnen, S. P. (2014). Altered structural networks and executive deficits in traumatic brain injury patients. *Brain Struct Funct*, *219*(1), 193-209.

Cruzat, J., Perl, Y. S., Escrichs, A., Vohryzek, J., Timmermann, C., Roseman, L., Luppi, A. I., Ibañez, A., Nutt, D., Carhart-Harris, R., Tagliazucchi, E., Deco, G., & Kringelbach, M. L. (2022). Effects of classic psychedelic drugs on turbulent signatures in brain dynamics. *Network Neuroscience*, *6*(4), 1104-1124.

De Filippi, E., Uribe, C., Avila-Varela, D. S., Martínez-Molina, N., Gashaj, V., Pritschet, L., Santander, T., Jacobs, E. G., Kringelbach, M. L., Sanz Perl, Y., Deco, G., & Escrichs, A. (2021). The Menstrual Cycle Modulates Whole-Brain Turbulent Dynamics. *Front Neurosci*, *15*, 753820.

Deco, G., Cabral, J., Saenger, V. M., Boly, M., Tagliazucchi, E., Laufs, H., Van Someren, E., Jobst, B., Stevner, A., & Kringelbach, M. L. (2018). Perturbation of whole-brain dynamics in silico reveals mechanistic differences between brain states. *Neuroimage*, *169*, 46-56.

Deco, G., Cruzat, J., Cabral, J., Tagliazucchi, E., Laufs, H., Logothetis, N. K., & Kringelbach, M. L. (2019). Awakening: Predicting external stimulation to force transitions between different brain states. *Proc Natl Acad Sci U S A*, *116*(36), 18088-18097.

Deco, G., & Kringelbach, M. L. (2014). Great expectations: using whole-brain computational connectomics for understanding neuropsychiatric disorders. *Neuron*, *84*(5), 892-905.

Deco, G., & Kringelbach, M. L. (2020). Turbulent-like Dynamics in the Human Brain. *Cell Rep*, *33*(10), 108471.

Deco, G., Kringelbach, M. L., Jirsa, V. K., & Ritter, P. (2017a). The dynamics of resting fluctuations in the brain: metastability and its dynamical cortical core. *Scientific Reports*, *7*(1), 3095.

Deco, G., Sanz Perl, Y., Vuust, P., Tagliazucchi, E., Kennedy, H., & Kringelbach, M. L. (2021). Rare long-range cortical connections enhance human information processing. *Curr Biol*, *31*(20), 4436-4448.e4435.

Deco, G., Tagliazucchi, E., Laufs, H., Sanjuán, A., & Kringelbach, M. L. (2017b). Novel Intrinsic Ignition Method Measuring Local-Global Integration Characterizes Wakefulness and Deep Sleep. *eNeuro*, *4*(5).

Deco, G., Tononi, G., Boly, M., & Kringelbach, M. L. (2015). Rethinking segregation and integration: contributions of whole-brain modelling. *Nat Rev Neurosci*, *16*(7), 430-439.

Demertzi, A., Antonopoulos, G., Heine, L., Voss, H. U., Crone, J. S., de Los Angeles, C., Bahri, M. A., Di Perri, C., Vanhaudenhuyse, A., Charland-Verville, V., Kronbichler, M., Trinka, E., Phillips, C., Gomez, F., Tshibanda, L., Soddu, A., Schiff, N. D., Whitfield-Gabrieli, S., & Laureys, S. (2015). Intrinsic functional connectivity differentiates minimally conscious from unresponsive patients. *Brain*, *138*(Pt 9), 2619-2631.

Demirtas-Tatlidede, A., Vahabzadeh-Hagh, A. M., Bernabeu, M., Tormos, J. M., & Pascual-Leone, A. (2012). Noninvasive Brain Stimulation in Traumatic Brain Injury. *The Journal of Head Trauma Rehabilitation*, *27*(4), 274-292.

Ercsey-Ravasz, M., Markov, N. T., Lamy, C., Van Essen, D. C., Knoblauch, K., Toroczkai, Z., & Kennedy, H. (2013). A predictive network model of cerebral cortical connectivity based on a distance rule. *Neuron*, *80*(1), 184-197.

Erika-Florence, M., Leech, R., & Hampshire, A. (2014). A functional network perspective on response inhibition and attentional control. *Nature communications*, *5*(1), 1-12.

Escrichs, A., Perl, Y. S., Uribe, C., Camara, E., Turker, B., Pyatigorskaya, N., Lopez-Gonzalez, A., Pallavicini, C., Panda, R., Annen, J., Gosseries, O., Laureys, S., Naccache, L., Sitt, J. D., Laufs, H., Tagliazucchi, E., Kringelbach, M. L., & Deco, G. (2022). Unifying turbulent dynamics framework distinguishes different brain states. *Commun Biol*, *5*(1), 638.

Fox, M. D., Snyder, A. Z., Vincent, J. L., Corbetta, M., Van Essen, D. C., & Raichle, M. E. (2005). The human brain is intrinsically organized into dynamic, anticorrelated functional networks. *Proc Natl Acad Sci U S A*, *102*(27), 9673-9678.

Friston, K. J. (1997). Transients, metastability, and neuronal dynamics. *Neuroimage*, *5*(2), 164-171.

Glerean, E., Salmi, J., Lahnakoski, J. M., Jaaskelainen, I. P., & Sams, M. (2012). Functional magnetic resonance imaging phase synchronization as a measure of dynamic functional connectivity. *Brain Connect*, *2*(2), 91-101.

Hellyer, P. J., Leech, R., Ham, T. E., Bonnelle, V., & Sharp, D. J. (2013). Individual prediction of white matter injury following traumatic brain injury. *Ann Neurol*, *73*(4), 489-499.

Hellyer, P. J., Scott, G., Shanahan, M., Sharp, D. J., & Leech, R. (2015). Cognitive Flexibility through Metastable Neural Dynamics Is Disrupted by Damage to the Structural Connectome. *J Neurosci*, *35*(24), 9050-9063.

Horn, A., & Blankenburg, F. (2016). Toward a standardized structural-functional group connectome in MNI space. *Neuroimage*, *124*(Pt A), 310-322.

Horn, A., Neumann, W. J., Degen, K., Schneider, G. H., & Kühn, A. A. (2017). Toward an electrophysiological "sweet spot" for deep brain stimulation in the subthalamic nucleus. *Hum Brain Mapp*, *38*(7), 3377-3390.

Jilka, S. R., Scott, G., Ham, T., Pickering, A., Bonnelle, V., Braga, R. M., Leech, R., & Sharp, D. J. (2014). Damage to the salience network and interactions with the default mode network. *Journal of Neuroscience*, *34*(33), 10798-10807.

Jolly, A. E., Bălăeţ, M., Azor, A., Friedland, D., Sandrone, S., Graham, N. S. N., Zimmerman, K., & Sharp, D. J. (2021). Detecting axonal injury in individual patients after traumatic brain injury. *Brain*, *144*(1), 92-113.

Kawamura, Y., Nakao, H., & Kuramoto, Y. (2007). Noise-induced turbulence in nonlocally coupled oscillators. Phys Rev E Stat Nonlin Soft Matter Phys, 75(3 Pt 2), 036209.

Kinnunen, K. M., Greenwood, R., Powell, J. H., Leech, R., Hawkins, P. C., Bonnelle, V., Patel, M. C., Counsell, S. J., & Sharp, D. J. (2011). White matter damage and cognitive impairment after traumatic brain injury. Brain, 134(2), 449-463.

Kringelbach, M. L., & Deco, G. (2020). Brain States and Transitions: Insights from Computational Neuroscience. *Cell Rep*, *32*(10), 108128.

Kuramoto, Y. (1984). Chemical turbulence, in: *Chemical oscillations, waves, and turbulence.* Springer Berlin, Heidelberg, pp. 111-140.

López-González, A., Panda, R., Ponce-Alvarez, A., Zamora-López, G., Escrichs, A., Martial, C., Thibaut, A., Gosseries, O., Kringelbach, M. L., Annen, J., Laureys, S., & Deco, G. (2021). Loss of consciousness reduces the stability of brain hubs and the heterogeneity of brain dynamics. *Communications Biology*, *4*(1), 1037.

Martinez-Molina, N., Siponkoski, S. T., Kuusela, L., Laitinen, S., Holma, M., Ahlfors, M., Jordan-Kilkki, P., Ala-Kauhaluoma, K., Melkas, S., Pekkola, J., Rodriguez-Fornells, A., Laine, M., Ylinen, A., Rantanen, P., Koskinen, S., Cowley, B. U., & Sarkamo, T. (2021). Resting-State Network Plasticity Induced by Music Therapy after Traumatic Brain Injury. *Neural Plast*, *2021*, 6682471.

Martinez-Molina, N., Siponkoski, S. T., & Sarkamo, T. (2022). Cognitive efficacy and neural mechanisms of music-based neurological rehabilitation for traumatic brain injury. *Ann N Y Acad Sci*, *1515*(1), 20-32.

McAllister, T. W., Flashman, L. A., Sparling, M. B., & Saykin, A. J. (2004). Working memory deficits after traumatic brain injury: catecholaminergic mechanisms and prospects for treatment -- a review. *Brain Inj*, *18*(4), 331-350.

Miyake, A., Friedman, N. P., Emerson, M. J., Witzki, A. H., Howerter, A., & Wager, T. D. (2000). The unity and diversity of executive functions and their contributions to complex "Frontal Lobe" tasks: a latent variable analysis. *Cogn Psychol*, *41*(1), 49-100.

Nardone, R., Sebastianelli, L., Versace, V., Brigo, F., Golaszewski, S., Manganotti, P., Saltuari, L., & Trinka, E. (2020). Repetitive transcranial magnetic stimulation in traumatic brain injury: Evidence from animal and human studies. *Brain Research Bulletin*, *159*, 44-52.

National Academies of Sciences, Engineering, and Medicine; Health and Medicine Division; Board on Health Care Services; Board on Health Sciences Policy; Committee on Accelerating Progress in Traumatic Brain Injury Research and Care. (2022). *Traumatic Brain Injury: A Roadmap for Accelerating Progress.* Matney, C., Bowman, K., & Berwick, D. (Eds.), National Academies Press, Washington DC.

Nieto-Castanon, A. (2020). *Handbook of functional connectivity Magnetic Resonance Imaging Methods in CONN*. Hilbert-Press, Boston, MA.

Ponsford, J. L., Downing, M. G., Olver, J., Ponsford, M., Acher, R., Carty, M., & Spitz, G. (2014). Longitudinal follow-up of patients with traumatic brain injury: outcome at two, five, and ten years post-injury. *J Neurotrauma*, *31*(1), 64-77.

Roy, A., Bernier, R. A., Wang, J., Benson, M., French, J. J., Jr, Good, D. C., & Hillary, F. G. (2017). The evolution of cost-efficiency in neural networks during recovery from traumatic brain injury. *PloS one*, 12(4), e0170541.

Schaefer, A., Kong, R., Gordon, E. M., Laumann, T. O., Zuo, X. N., Holmes, A. J., Eickhoff, S. B., & Yeo, B. T. T. (2018). Local-Global Parcellation of the Human Cerebral Cortex from Intrinsic Functional Connectivity MRI. Cereb Cortex, 28(9), 3095-3114.

Setsompop, K., Kimmlingen, R., Eberlein, E., Witzel, T., Cohen-Adad, J., McNab, J. A., Keil, B., Tisdall, M. D., Hoecht, P., Dietz, P., Cauley, S. F., Tountcheva, V., Matschl, V., Lenz, V. H., Heberlein, K., Potthast, A., Thein, H., Van Horn, J., Toga, A., . . . Wald, L. L. (2013). Pushing the limits of in vivo diffusion MRI for the Human Connectome Project. *Neuroimage*, *80*, 220-233.

Shanahan, M. (2010). Metastable chimera states in community-structured oscillator networks. *Chaos*, *20*(1), 013108.

Sharp, D. J., Bonnelle, V., De Boissezon, X., Beckmann, C. F., James, S. G., Patel, M. C., & Mehta, M. A. (2010). Distinct frontal systems for response inhibition, attentional capture, and error processing. *Proc Natl Acad Sci U S A*, *107*(13), 6106-6111.

Sharp, D. J., Scott, G., & Leech, R. (2014). Network dysfunction after traumatic brain injury. *Nat Rev Neurol*, *10*(3), 156-166.

Sihvonen, A. J., Siponkoski, S.-T., Martínez-Molina, N., Laitinen, S., Holma, M., Ahlfors, M., Kuusela, L., Pekkola, J., Koskinen, S., & Särkämö, T. (2022). Neurological Music Therapy Rebuilds Structural Connectome after Traumatic Brain Injury: Secondary Analysis from a Randomized Controlled Trial. *Journal of Clinical Medicine*, *11*(8), 2184.

Siponkoski, S. T., Koskinen, S., Laitinen, S., Holma, M., Ahlfors, M., Jordan-Kilkki, P., Ala-Kauhaluoma, K., Martinez-Molina, N., Melkas, S., Laine, M., Ylinen, A., Zasler, N., Rantanen, P., Lipsanen, J., & Sarkamo, T. (2021). Effects of neurological music therapy on behavioural and emotional recovery after traumatic brain injury: A randomized controlled cross-over trial. *Neuropsychol Rehabil*, 32(7),1356-1388.

Siponkoski, S. T., Martinez-Molina, N., Kuusela, L., Laitinen, S., Holma, M., Ahlfors, M., Jordan-Kilkki, P., Ala-Kauhaluoma, K., Melkas, S., Pekkola, J., Rodriguez-Fornells, A., Laine, M., Ylinen, A.,

Rantanen, P., Koskinen, S., Lipsanen, J., & Särkämö, T. (2020). Music Therapy Enhances Executive Functions and Prefrontal Structural Neuroplasticity after Traumatic Brain Injury: Evidence from a Randomized Controlled Trial. *J Neurotrauma*, *37*(4), 618-634.

Spreng, R. N., & Grady, C. L. (2010). Patterns of brain activity supporting autobiographical memory, prospection, and theory of mind, and their relationship to the default mode network. *Journal of Cognitive Neuroscience*, *22*(6), 1112-1123.

Tognoli, E., & Kelso, J. A. (2014). The metastable brain. *Neuron*, *81*(1), 35-48.

Van Dijk, K. R., Hedden, T., Venkataraman, A., Evans, K. C., Lazar, S. W., & Buckner, R. L. (2010). Intrinsic functional connectivity as a tool for human connectomics: theory, properties, and optimization. *J Neurophysiol*, *103*(1), 297-321.

Yang, L., Wei, J., Li, Y., Wang, B., Guo, H., Yang, Y., & Xiang, J. (2021). Test-Retest Reliability of Synchrony and Metastability in Resting State fMRI. *Brain Sci*, *12*(1).

Figures

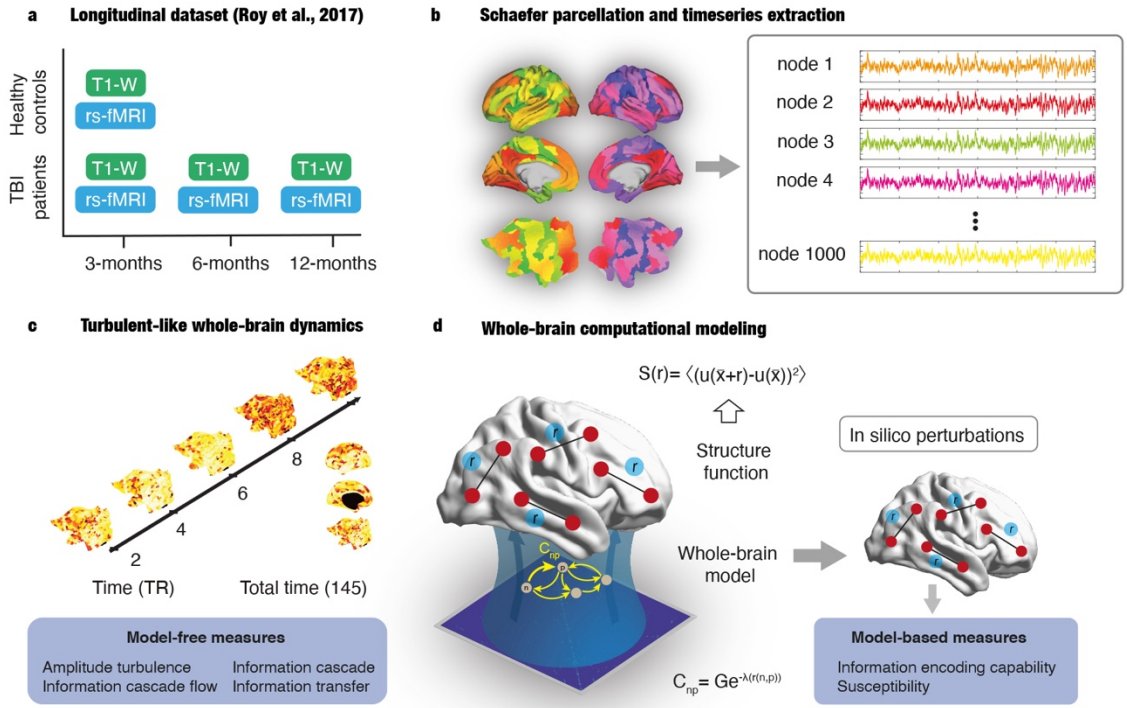

Figure 1: Overview of experimental data acquisition as well as the model-free and model-based analysis pipelines.

(a) We used an open access longitudinal dataset from a previous publication (Roy et al., 2017). T1-weighted (T1-W) and resting state fMRI (rs-fMRI) data from traumatic brain injury (TBI) patients were collected at three time points (3-, 6- and 12-months post-injury). For group comparisons, T1-W and rs-fMRI were collected from age-matched healthy controls. **(b)** rs-fMRI data were preprocessed in the CONN toolbox and the timeseries were extracted for each of the 1,000 nodes in the Schaefer parcellation (Schaefer et al, 2018). **(c)** Model-free approach. Visualization of the change over time and space of the Kuramoto local order parameter in a healthy subject (left hemisphere). The Kuramoto local order parameter can define the turbulent signatures of brain activity at different spatial scales in the vortex space. Here, we computed four turbulent measures based on the Kuramoto local order parameter to characterize the brain's information processing: amplitude turbulence, information cascade flow, information cascade and information transfer (see Methods for more details). **(d)** Model-based approach. We built Hopf whole-brain dynamical models that described the intrinsic dynamics of each brain area by a Stuart-Landau non-linear oscillator. Such local oscillators are linked through the underlying structural connectivity to simulate the global dynamics. We used the DTI matrix with the exponential distance rule as structural connectivity to fit the empirical data as a function of the Euclidean distance. Then we applied *in silico* perturbations to assess the model's reaction for each time point in the TBI group compared to healthy controls using the susceptibility and information encoding capability model-based measures (panels c and d adapted with permission from Deco & Kringelbach, 2020).

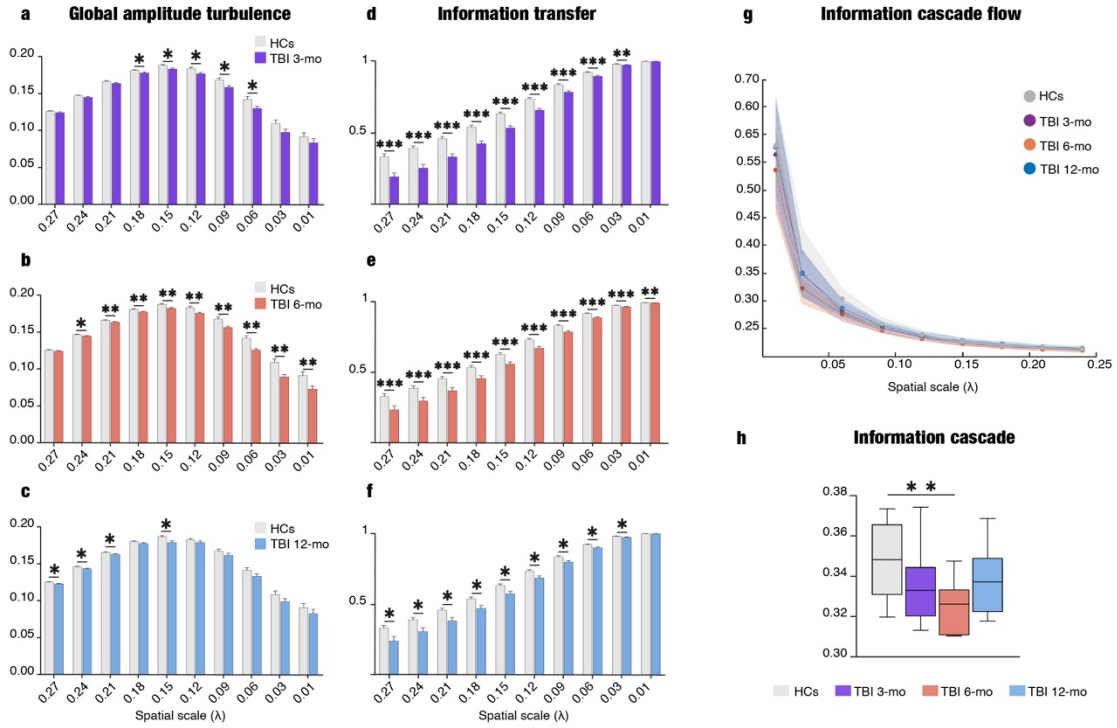

Figure 2: Global amplitude turbulence differs between TBI patients and healthy controls over time, peaking at 6-months for large distance scales.

Significant differences were found in turbulent-like dynamics between healthy controls (HCs) and TBI patients at 3-, 6- and 12-months post-injury. **(a-c)** Mean amplitude turbulence (+SEM). Differences between HCs and TBI patients in amplitude turbulence at larger distances (smaller λ values) are significant at 6-months post-injury and recover after 12-months. **(d-e)** Mean information transfer (+SEM). HCs and TBI patients at all time points show significant differences across most **(d,f)** or all **(e)** λ spatial scales. **(g)** For information cascade flow, the largest effect size was found at λ=0.06 in the HCs vs TBI after 6-months comparison. **(h)** TBI patients at 6-months post-injury showed decreased values of information cascade as compared to HCs. The lower and upper edges of the box indicate the first (25th percentile) and third quartile (75th percentile), middle lines are medians (*$p < 0.05$, **$p < 0.01$, ***$p < 0.001$, after FDR correction including all computed λ).

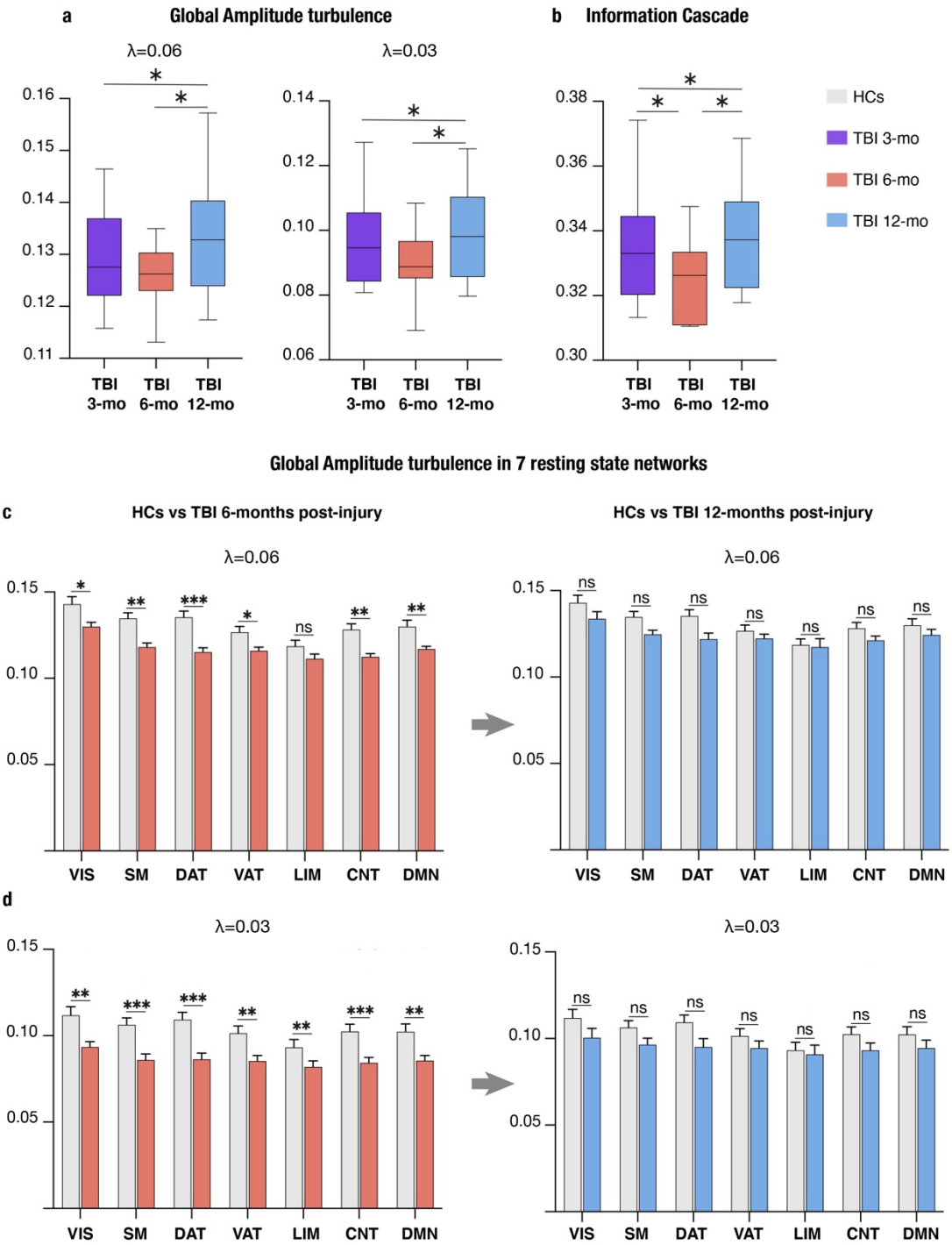

Figure 3: TBI patients exhibit significant changes in network-level amplitude turbulence at 6-months but show recovery at 12-months.

Longitudinal changes in amplitude turbulence, information cascade flow and information cascade in TBI patients and network-level turbulence recovery at large distances**. (a)** TBI patients at 6-months post-injury showed decreased values of amplitude turbulence at λ = 0.06 and λ =0.03 as compared to the 12-months post-injury stage. **(b)** Information cascade in TBI patients is reduced at 6-months post-injury compared to 3- and 12-months stages. The lower and upper edges of the box indicate the first (25th percentile) and third quartile (75th percentile), middle lines are medians. **(c)** Amplitude turbulence at 6-months post-injury is reduced as compared to healthy controls in most RSNs at λ = 0.06 (left) but recovers after 12-months post-injury (right). **(d)** Likewise, the differences in amplitude turbulence are no longer significant when comparing healthy controls to TBI patients at 12-months post-injury at λ = 0.03. Abbreviations: LIM, limbic; CNT, control; DMN, default mode; DAT, dorsal-attention; VAT, ventral attention; VIS, visual; SM, somatosensory (* $p < 0.05$, ** $p < 0.01$, *** $p < 0.001$, after FDR correction including all computed λ).

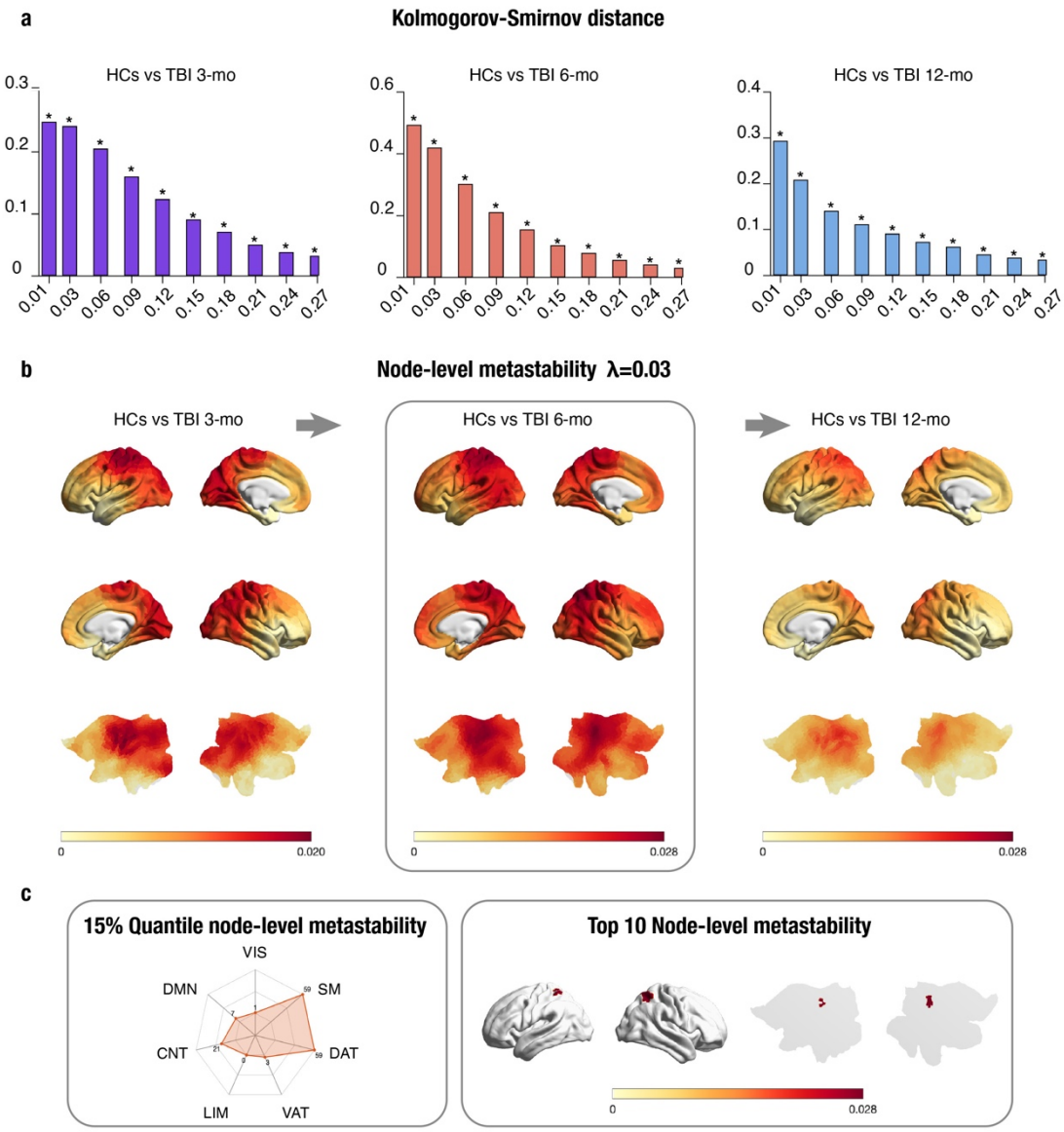

Figure 4: Nodes in the somatosensory, dorsal attention and control networks show the highest difference in TBI patients at 6-months post-injury.

(a) Kolmogorov-Smirnov distance (KSD) distributions for the difference in node-level turbulence between healthy controls (HCs) and TBI patients at 3- (left), 6- (middle) and 12-months post-injury. Of note, the largest KSD values were reached for lower λ values (large distances) at the 6-months post-injury stage (right). (b) Render brains represent the absolute difference of the node-level metastability between each dataset for scale λ = 0.03. (c) Left: Radar plot representing the number of nodes on the top 15% quantile of the absolute difference for the HCs vs TBI patients at 6-months post-injury comparison at λ =0.03. Most of the nodes were ascribed to the SM, DAT and CNT networks. Right: The top 10 nodes from the Schaefer parcellation within the top 15 % quantile above mentioned were located in the LH SM and bilateral DAT networks. Abbreviations: LH: left hemisphere; LIM, limbic; CNT, control; DMN, default mode; DAT, dorsal-attention; VAT, ventral attention; VIS, visual; SM, somatosensory (* $p < 0.001$, after FDR correction including all computed λ).

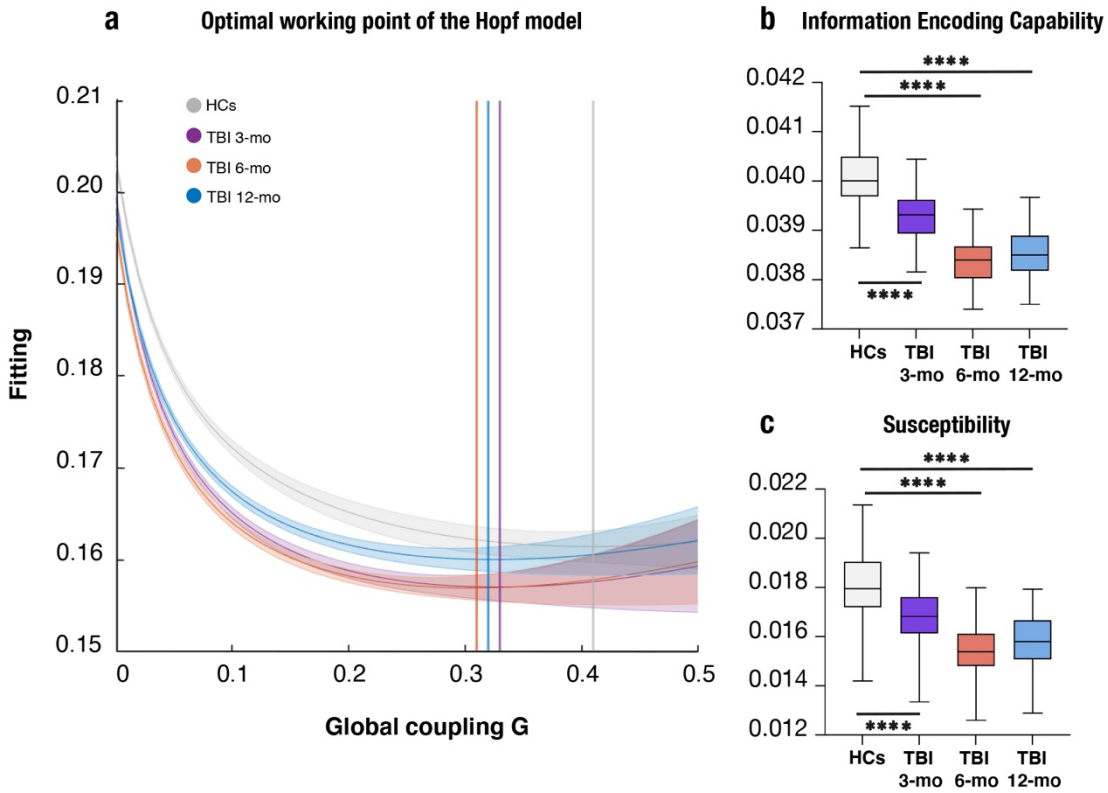

Figure 5: TBI patients show reduced reactivity to *in silico* perturbations over time with the lowest value at 6-months post-injury.

Model-based framework revealed significant perturbative differences between healthy controls (HCs) and TBI patients across all time points. **(a)** Evolution of the error of fitting the whole-brain model to the rs-fMRI data as a function of the global coupling strength, G. The optimal working point fitting the TBI data was lower than that for HCs. The shadow indicates the SEM. **(b)** Information encoding capability and **(c)** susceptibility measures were significantly reduced in the pairwise comparison between HCs and TBI patients across all three time points. The lower and upper edges of the box indicate the first (25th percentile) and third quartile (75th percentile), middle lines are medians (*** $p < 0.001$, after FDR correction).

Supplementary Material

Table S1. Amplitude Turbulence in HCs vs TBI at 3-months post-injury

λ value	$t_{(22)}$	p-val	Effect size (Cohen's d)	p-adj
0.27	1.734	0.096974	0.683308	0.108827
0.24	1.942	0.064994	0.765597	0.083664
0.21	2.225	0.036626	0.877092	0.061654
0.18	2.545	0.018457	1.003077	0.037283
0.15	2.773	0.011084	1.093115	0.037283
0.12	2.867	0.008948	1.130188	0.037283
0.09	2.857	0.009175	1.125886	0.037283
0.06	2.645	0.014790	1.042513	0.037283
0.03	1.933	0.066269	0.761699	0.083664
0.01	1.059	0.301211	0.417290	0.304223

Table S2. Amplitude Turbulence in HCs vs TBI at 6-months post-injury

λ value	$t_{(22)}$	p-val	Effect size (Cohen's d)	p-adj
0.27	1.422	0.168928	0.560639	0.068247
0.24	1.906	0.069788	0.751270	0.031327
0.21	2.553	0.018153	1.006054	0.009167
0.18	3.107	0.005140	1.224624	0.003461
0.15	3.302	0.003246	1.301477	0.002623
0.12	3.446	0.002306	1.358081	0.002329
0.09	3.684	0.001299	1.452025	0.002223
0.06	3.889	0.000790	**1.532945**	0.002223
0.03	3.585	0.001651	1.412946	0.002223
0.01	2.717	0.012581	1.070993	0.007261

Table S3. Amplitude Turbulence in HCs vs TBI at 12-months post-injury

λ value	$t_{(22)}$	p-val	Effect size (Cohen's d)	p-adj
0.27	2.775	0.011049	1.093671	0.037199
0.24	2.818	0.010022	1.110612	0.037199
0.21	2.617	0.015744	1.031438	0.039754
0.18	2.089	0.048538	0.823173	0.098047
0.15	3.315	0.003149	0.618023	0.031804
0.12	1.357	0.188632	0.534740	0.211687
0.09	1.462	0.157871	0.576251	0.199312
0.06	1.632	0.116993	0.643093	0.186837
0.03	1.575	0.129491	0.620841	0.186837
0.01	1.050	0.305033	0.413924	0.308083

Table S4. Information transfer in HCs vs TBI at 3-months post-injury

λ value	$t_{(22)}$	p-val	Effect size (Cohen's d)	p-adj
0.27	4.487	0.000183	1.768704	0.000053
0.24	4.654	0.000122	1.834160	0.000041
0.21	4.924	0.000063	1.940726	0.000032
0.18	5.206	0.000032	2.051966	0.000022
0.15	5.473	0.000017	2.157027	0.000017
0.12	5.516	0.000015	2.173964	0.000017
0.09	4.728	0.000102	1.863512	0.000041
0.06	3.719	0.001193	1.465938	0.000301
0.03	2.274	0.033054	0.896393	0.007419
0.01	0.6034	0.552432	0.237815	0.111591

Table S5. Information transfer in HCs vs TBI at 6-months post-injury

λ value	$t_{(22)}$	p-val	Effect size (Cohen's d)	p-adj
0.27	2.891	0.008471	1.139628	0.000951
0.24	3.075	0.005545	1.211813	0.000700
0.21	3.284	0.003386	1.294477	0.000489
0.18	3.542	0.001830	1.396035	0.000308
0.15	3.800	0.000982	1.497596	0.000248
0.12	4.017	0.000579	1.583283	0.000195
0.09	4.148	0.000421	1.634829	0.000195
0.06	4.210	0.000361	**1.659254**	0.000195
0.03	3.635	0.001462	1.432820	0.000295
0.01	2.062	0.051240	0.812626	0.005175

Table S6. Information transfer in HCs vs TBI at 12-months post-injury

λ value	$t_{(22)}$	p-val	Effect size (Cohen's d)	p-adj
0.27	2.586	0.016849	1.019369	0.021272
0.24	2.638	0.015022	1.039760	0.021272
0.21	2.689	0.013402	1.059889	0.021272
0.18	2.768	0.011226	1.090910	0.021272
0.15	2.858	0.009136	1.126621	0.021272
0.12	2.984	0.006842	1.176171	0.021272
0.09	3.076	0.005530	1.212285	0.021272
0.06	3.082	0.005450	1.214725	0.021272
0.03	2.314	0.030420	0.911894	0.034138
0.01	0.9103	0.372550	0.358774	0.376275

Table S7. Information cascade flow in HCs vs TBI at 3-months post-injury

λ value	$t_{(22)}$	p-val	Effect size (Cohen's d)	p-adj
0.27	1.350	0.190851	0.531959	0.216855
0.24	1.704	0.102470	0.531959	0.155242
0.21	2.237	0.035745	0.671613	0.064984
0.18	2.818	0.010018	0.881690	0.030355
0.15	3.168	0.004451	1.110682	0.030355
0.12	2.994	0.006687	1.248823	0.030355
0.09	2.346	0.028391	1.180058	0.064519
0.06	1.588	0.126649	0.924691	0.164462
0.03	0.9188	0.368162	0.625738	0.371843
0.01	1.350	0.190851	0.362141	0.216855

Table S8. Information cascade flow in HCs vs TBI at 6-months post-injury

λ value	$t_{(22)}$	p-val	Effect size (Cohen's d)	p-adj
0.27	1.280	0.213815	0.504576	0.119974
0.24	1.670	0.109104	0.504576	0.068872
0.21	2.164	0.041627	0.658189	0.030031
0.18	2.808	0.010237	0.852763	0.010340
0.15	3.457	0.002245	1.106930	0.002835
0.12	4.121	0.000449	1.362441	0.001134
0.09	4.413	0.000220	1.624239	0.001110
0.06	3.680	0.001311	**1.739470**	0.002207
0.03	2.520	0.019494	1.450571	0.016408
0.01	1.280	0.213815	0.993252	0.119974

Table S9. Information cascade flow in HCs vs TBI at 12-months post-injury

λ value	$t_{(22)}$	p-val	Effect size (Cohen's d)	p-adj
0.27	0.09352	0.926334	0.036862	0.935598
0.24	0.4091	0.686395	0.036862	0.779916
0.21	0.8870	0.384698	0.161259	0.582818
0.18	1.481	0.152688	0.349586	0.346984
0.15	2.010	0.056904	0.583875	0.173095
0.12	2.321	0.029959	0.792043	0.173095
0.09	2.008	0.057127	0.914733	0.173095
0.06	1.300	0.206953	0.791271	0.376240
0.03	0.7222	0.477795	0.512509	0.620450
0.01	0.09352	0.926334	0.284640	0.935598

Tabla S10. Information cascade

Group comparison	$t_{(22)}$	p-val	Effect size (Cohen's d)
HCs vsTBI 3-months	1.642	0.1148	0.647208
HCs vs TBI 6-months	3.449	0.0023	**1.359255**
HCs vs TBI 12-months	1.271	0.2169	0.501097

Tabla S11. Amplitude turbulence by resting state network (RSN) in HCs vs TBI at 6-months post-injury at λ=0.06

RSN	$t_{(22)}$	p-val	Effect size (Cohen's d)	p-adj
VIS	2.557	0.020186	1.007643	0.013592
SM	4.048	0.000621	**1.595308**	0.001060
DAT	4.515	0.000214	**1.779683**	0.000864
VAT	2.727	0.013728	1.074843	0.011092
LIM	1.605	0.123527	0.632678	0.071293
CNT	4.047	0.000787	**1.595079**	0.001060
DMN	3.130	0.006930	1.233561	0.006999

Tabla S12. Amplitude turbulence by resting state network (RSN) in HCs vs TBI at 6-months post-injury at λ=0.03

RSN	$t_{(22)}$	p-val	Effect size (Cohen's d)	p-adj
VIS	3.084	0.006292	1.215555	0.001105
SM	3.761	0.001102	**1.482488**	0.000556
DAT	4.060	0.000546	**1.600150**	0.000552
VAT	3.023	0.006566	1.191591	0.001105
LIM	1.954	0.064311	0.770056	0.009279
CNT	3.434	0.002622	**1.353555**	0.000883
DMN	3.126	0.005525	1.232278	0.001105

Tabla S13. Top 10 nodes in amplitude turbulence for HCs vs TBI at 6-months post-injury at λ=0.03

Schaefer 1000 nodes label	Anatomical region
727	7Networks_RH_DorsAttn_Post_43\
716	7Networks_RH_DorsAttn_Post_32\
728	7Networks_RH_DorsAttn_Post_44\
219	7Networks_LH_DorsAttn_Post_47\
733	7Networks_RH_DorsAttn_Post_49\
718	7Networks_RH_DorsAttn_Post_34\
729	7Networks_RH_DorsAttn_Post_45\
140	7Networks_LH_SomMot_59\
726	7Networks_RH_DorsAttn_Post_42\

160	7Networks_LH_SomMot_79\
727	7Networks_RH_DorsAttn_Post_43\
716	7Networks_RH_DorsAttn_Post_32\

Tabla S14. Susceptibility and information encoding capability in HCs vs TBI

Susceptibility				
Group comparison	**$t_{(198)}$**	**p-val**	**Effect size (Cohen's d)**	**p-adj**
HCs vs TBI 3mo	10.030	<0.0001	1.412904	<0.0001
HCs vs TBI 6mo	23.300	<0.0001	**3.282681**	<0.0001
HCs vs TBI 12mo	20.870	<0.0001	2.940224	<0.0001
Information encoding capability				
Group comparison	**$t_{(198)}$**	**p-val**	**Effect size (Cohen's d)**	**p-adj**
HCs vs TBI 3mo	6.936	<0.0001	0.977160	<0.0001
HCs vs TBI 6mo	15.42	<0.0001	**2.172492**	<0.0001
HCs vs TBI 12mo	13.72	<0.0001	1.932878	<0.0001

Description of additional supplementary files

File name: Video S1

Description: Spatiotemporal evolution of turbulence in a representative healthy control participant at λ = 0.03. The video shows the change over time and space of the Kuramoto local order parameter, R, rendered into the inflated 3D side and midline views as well as flat maps of both hemispheres (from top to bottom). The global amplitude turbulence for this participant was D = 0.133.

File name: Video S2-4

Description: Spatiotemporal evolution of turbulence in a representative TBI patient at 3-months (video S2), 6-months (video S3) and 12-months (video S4) post-injury at λ = 0.03. The video shows the change over time and space of the Kuramoto local order parameter, R, rendered into the inflated 3D side and midline views as well as flat maps of both hemispheres (from top to bottom). The global amplitude turbulence for this TBI patient was D=0.101 (3-months), D=0.069 (6-months) and D=0.098 (12-months).